Supplementary Information for

Supramolecular hydrogen-bonded chiral networks enable blue circularly polarized emission from polymeric carbon quantum dots

Sourav Mal[a,b], Youngsin Park[c], Deblina Das[b], Abhisheek Meena[d], Yongcheol Jo[e], Kwangseuk Kyhm[e], Robert A. Taylor[f], Atanu Jana[a,b*], Sangeun Cho[a,b*]

[a]Department of Semiconductor Science, Dongguk University, Seoul 04620, Republic of Korea
[b]Division of System Semiconductor, Dongguk University, Seoul 04620, Republic of Korea
[c]Department of Chemistry, School of Natural Science, Ulsan National Institute of Science and Technology (UNIST), Ulsan 44919, Republic of Korea
[d]CSIR - Central Electrochemical Research Institute, Karaikudi - 630003, Tamil Nadu, India
[e]Department of Opto-mechatronics Engineering, Pusan National University, Busan 46241, South Korea
[f]Clarendon Laboratory, Department of Physics, University of Oxford, Oxford, OX1 3PU, UK

Characterization methods

Zeta potential measurements were performed using a Zetasizer (ELSZ-2000, Otsuka Electronics). Field-emission scanning electron microscopy (FE-SEM) was conducted on a CLARA LMH system (TESCAN Brno), while high-resolution transmission electron microscopy (HRTEM) images were acquired using a JEM-2100F microscope (JEOL). Proton nuclear magnetic resonance (^{1}H NMR) spectra were recorded on a 500 MHz Fourier-transform NMR spectrometer (Bruker). X-ray photoelectron spectroscopy (XPS) and Fourier-transform infrared spectroscopy (FTIR) analyses were carried out using an ESCA XPS system and an ATR-FTIR spectrometer (Smiths Detection), respectively. Raman spectra were obtained using a JASCO NRS-4500 Raman spectrometer. UV–vis absorption and photoluminescence (PL) spectra were measured using Jasco V-770 and FP-8500 spectrophotometers, respectively. Chiroptical properties were assessed by circularly polarized luminescence (CPL-300, JASCO) and circular dichroism (CD, J-1000 series, JASCO) spectrometers.

Theoretical Background for Chiroptical Measurements

The circular dichroism (CD) phenomenon can be expressed quantitatively through the difference in molar extinction coefficients between right and left circularly polarized light (from the viewer's point)

$$\Delta_\epsilon = \epsilon_R - \epsilon_L \quad \text{..... (S1)}$$

where ϵ_R and ϵ_L represent the molar extinction coefficients for right and left circularly polarized light, respectively.

This difference characterizes the material's chiral optical activity.

CD measurements are typically reported as ellipticity (θ) in millidegrees,[1] related to Δ_ϵ by

$\theta = 32.98\Delta_\epsilon$ (independent of concentration and path length)

$\theta = 3298\Delta_\epsilon$ (units of degrees.cm^2·dmol^{-1})

$$\theta = \frac{3298 . \Delta_\epsilon}{wavelength\ (nm)} \quad \text{..... (S2)}$$

The dissymmetry factor or anisotropy factor (g_{abs}) provides a normalized measure of CD strength[2]

$$g_{abs} = \frac{CD}{A} = \frac{A_R - A_L}{\frac{A_R + A_L}{2}} = \frac{\Delta A}{A}$$ ..... (S3)

where $\Delta A = A_R - A_L$ is the difference in absorbance between right (A_R) and left (A_L) circularly polarized light, and $A = \frac{A_R + A_L}{2}$ is the average absorbance.

In terms of molar extinction coefficients, this can be expressed as

$$g_{abs} = \frac{CD}{A} = \frac{\epsilon_R - \epsilon_L}{\frac{\epsilon_R + \epsilon_L}{2}} = \frac{\Delta \epsilon}{\epsilon}$$ ..... (S4)

The optical rotatory dispersion (ORD) and CD are connected through the Kramers-Kronig relations, which link the real (n) and imaginary (k) parts of a material′s refractive index:

$$n(\lambda) - 1 = \frac{\lambda}{\pi} \int_0^\infty \frac{\Delta k(\lambda')}{\lambda'^2 - \lambda^2} d\lambda'$$ ..... (S5)

where $n(\lambda)$ represents the refractive index difference responsible for ORD, and $\Delta k(\lambda')$ is proportional to the CD spectrum.

For emission-based measurements, the luminescence dissymmetry factor (g_{lum}) quantifies the degree of circular polarization in luminescence,[3–5]

$$g_{lum} = \frac{2(I_R - I_L)}{(I_R + I_L)}$$ ..... (S6)

From the receiver's perspective, I_R and I_L are the intensities of right and left-handed circularly polarized emitted light, respectively.

The sign of the luminescence dissymmetry factor depends on the reference frame used to define circular polarization. In this work, $g_{lum}$is expressed according to the detector (receiver) perspective of the CPL instrument. Under this convention, a positive g_{lum} corresponds to dominant right-handed circularly polarized (RCP**)** emission and a negative g_{lum} corresponds to dominant left-handed circularly polarized (LCP**)** emission.[6,7]

Titration procedure: R/S-CPQ (5-30 mg) was dissolved in 1 mL of ethanol. Separately, PCQDs (0.185 g) were dispersed in 10 mL of water (18.5 mg mL^{-1}). Subsequently, 1 mL of

the CPQ solution was added to 4 mL of the PCQD dispersion (containing 74 mg PCQDs) under continuous stirring and mixed for 1 h to obtain R/S-CPQ@PCQDs. The CPQ loading was systematically controlled by varying the CPQ amount from 5 to 30 mg while maintaining a constant PCQD concentration.

Time-resolved photoluminescence (TRPL) for PCQDs with their Chiral inducer

The fluorescence lifetime of the PCQDs was determined according to an established method with the following equation:[8]

$$\tau_{avg} = \frac{\sum \alpha_i \tau_i^2}{\sum \alpha_i \tau_i}$$

PCQDs display biexponential decay kinetics, comprising a fast component (τ_1= 0.45 ns) attributed to surface trap-assisted quenching, and a slower component (τ_2 = 7.25 ns) arising from radiative recombination of excitons, yielding an average lifetime of 4.85 ns (Table S3). Functionalization with R- or S-**CPQ** markedly alters these dynamics. For R-**CPQ**@PCQDs, free excitons (τ_1) extends to 0.93 ns, while self-trapped excitons (τ_2) employs 5.59 ns, leading to a shortened τ_{avg} of 3.46 ns. The S-**CPQ**@PCQDs yields τ_1= 0.98 ns and τ_2=5.99 ns, with a marginally longer τ_{avg} of 3.85 ns. These variations propose the emergence of self-trapped exciton (STE) states facilitated by supramolecular charge-transfer interactions between the PCQDs core and quinone moieties of **CPQ**. The elongation in τ_2 indicates enhanced radiative recombination rates from stabilized STE states, while the reduction of τ_1 point to suppression of trap-mediated quenching-likely due to hydrogen-bonded surface passivation by the **CPQ** ligands. Despite reduced lifetimes, both systems exhibit enhanced CPL activity (g_{lum} =10^{-2}), indicating that chiral ligand binding accelerates radiative recombination within an asymmetric charge-transfer framework.[9,10]

Electrochemical Measurements

In the present study, CV scans were conducted on a 0.1 mg/ml aqueous dispersed solution of PCQDs in the presence of 0.1 M KCl by employing a state-of-the-art biological science instrument. The electrochemical cell was utilized in the experiments featured a Pt wire as the counter electrode, blank graphite as the working electrode, and a Hg/HgO reference electrode. The voltage scan range was kept for the experiments spanned -2 to 0.5 V, with a scan rate of 50 mV/s. These electrochemical conditions were carefully selected to ensure comprehensive and accurate data acquisition. The band positions of both PCQDs and R/S-**CPQ**@PCQDs were determined by the analysis of the oxidation (E_{ox}) and reduction (E_{red}) potentials from obtained cyclic voltammetry (CV) graph. This experimental setup, characterised by meticulous electrode selection and controlled electrochemical parameters, enabled precise elucidation of the band positions of PCQDs and their modified counterparts, R/S-**CPQ**@PCQDs. The obtained results provide valuable insights into the understanding of the electrochemical behavior of PCQDs and their functionalised derivatives, paving the way for further exploration in diverse applications.

In 50 ml of distilled water, 0.1 M KCl = 373 mg KCl (Mol. wt. = 74.55/mol) was dissolved. 1 ml of PCQDs was added to 50 ml of the 0.1 M KCL solution. Cyclic voltammetry was recorded against this electrolyte.

The energy levels of the PCQDs, referred to as their highest occupied molecular orbital (HOMO) and lowest unoccupied molecular orbital (LUMO), were evaluated by electrochemical studies. The cyclic voltammograms of the PCQDs were supported on Hg/HgO electrodes with varying scan speeds. Then, using the following well-known equation, HOMO and LUMO in electron volts can be computed.

$$E_{HOMO} = -e\left[E_{1/2_{red}} + 4.4\ V\right] \quad \ldots. (1)$$

$$E_{LUMO} = E_{HOMO} + E_g(Optical) \quad \ldots. (2)$$

According to Hereinafter[11] E_{HOMO} was determined from the oxidation potential with the value of -5.05 eV, but E_{LUMO} could not be computed because of the irreversibility of the reduction peak. However, the optical bandgap (E_g) can be calculated using optical data. An energy gap of 3.54 eV was observed for PCQDs. After incorporating the R/S-**CPQ** into the PCQD matrix, the band energy gap decreased compared to pure PCQDs.

Customised liquid polarizer fabrication method

A 100 µL of achiral PCQDs and COBCs (R/S-**CPQ**@PCQDs) was individually transferred into 20 mL vials. Controlled dilution was then performed by gradually adding di-water in a stepwise manner, increasing the total volume from 100 µL to 1000 µL, ensuring precise kinetics. A display chamber with a thickness of 1.5 mm and a hollow interior was prepared. The prepared solutions of COBCs and achiral PCQDs were poured into the display chamber, filling it completely.

To assess the image quality resolution, a UV LED light source was positioned at 4.5 cm, an appropriate distance behind an image within a dark chamber to ensure controlled lighting conditions. The display film, filled with either the chiral or achiral PCQD solution, was placed in front of the image. The resolution of the image transmitted through the filled display film was recorded and subsequently analyzed for quality evaluation. Image pixel quality was measured by the spatial resolution lp/mm techniques.

Calculation of the absolute PL QY

The quantum yield was measured using the FP-8500 spectrofluorometer (JASCO). The absolute PL QY can be calculated using the following equation:

$$\text{PLQY} = \frac{S_2}{S_0 - S_1} \times 100,$$
$$= 67.54\%.$$

$\mathbf{S_2}$ denotes the emission intensity collected from the sample within the integrating sphere; $\mathbf{S_1}$ represents the scattering signal from the PCQD sample, also measured using the integrating sphere; and $\mathbf{S_0}$ corresponds to the excitation light spectrum recorded with only the solvent inside the sphere. In this study, distilled water served as the solvent. For R/S-**CPQ**@PCQDs, P L QY was recorded using a water-ethanol solvent mixture.

Supplementary figures

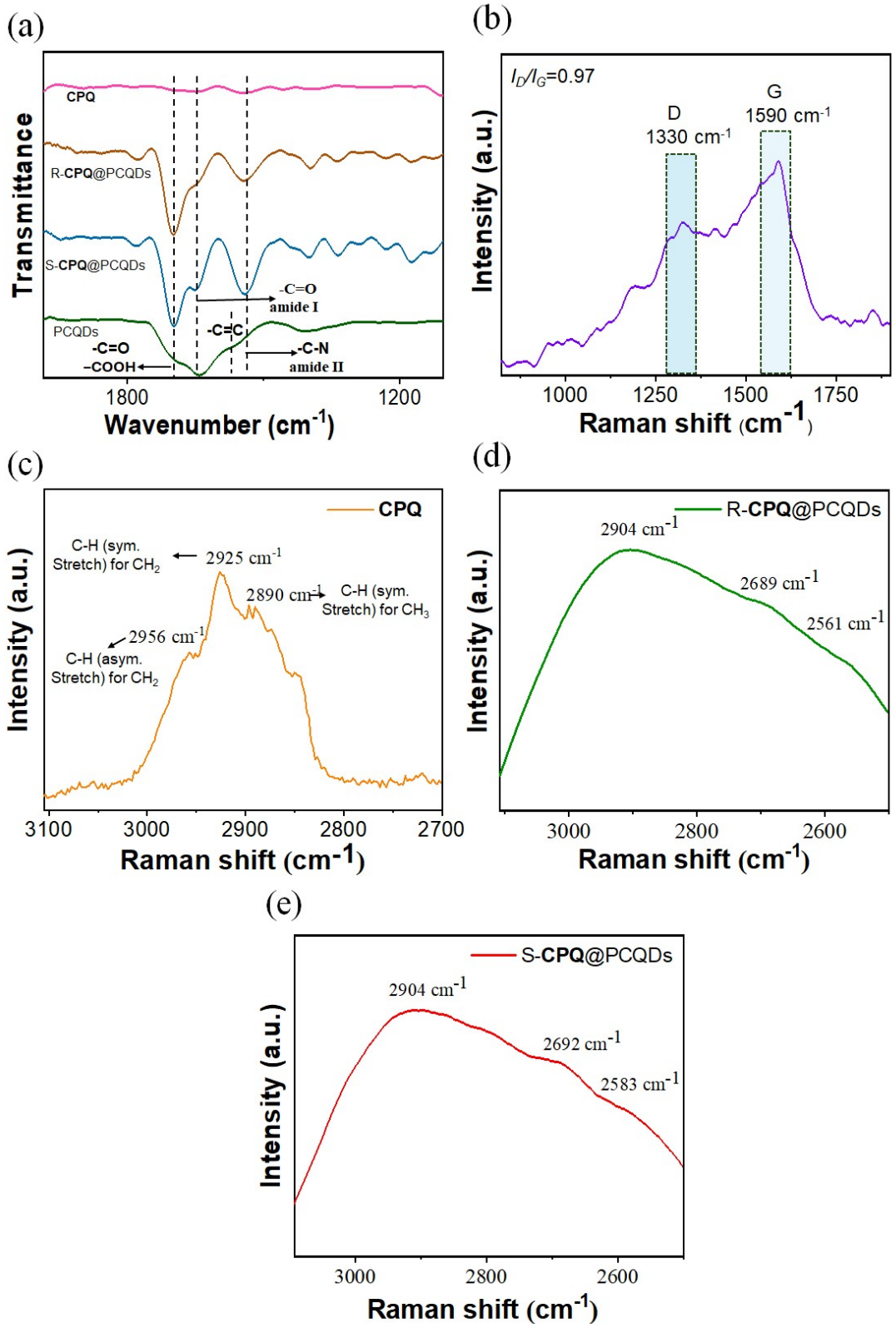

Fig. S1. (a) Enlarged FTIR spectra of pristine PCQDs and R/S-CPQ@PCQD composites (COBCs) in the 1800-1200 cm^{-1} range, highlighting the characteristic bands of carbonyl (-C=O/-COOH), amide I, amide II/C-N, and conjugated C=C groups, Raman spectra of (b) pure

PCQDs, (c) **CPQ**, (d) R-**CPQ**@PCQDs, and (e) S-**CPQ**@PCQDs, revealing distinctive carbon-based vibrational features.

Raman tests were conducted in order to verify the carbon nature of PCQDs. Here, the pure CQDs sample revealed two discernible bands at 1330 (D-band) and 1590 cm^{-1} (G-band) as depicted in Fig. S1b. The G band within amorphous carbon stems from in-plane vibrations, which carbon atoms with sp^2 hybridization demonstrate. The broadening and spectral position changes of the G band become pronounced because amorphous carbon contains inherent structural disorder compared to crystalline graphitic materials. The intensity measurement for the D-band compared to the G-band (I_D/I_G) yielded a value of 0.97 for PCQDs. The very high I_D/I_G ratio provides strong evidence of minimum graphitic structure formation within this material structure.[12] The synthesized PCQD structure contains significant amounts of amorphous carbon which can be determined through this ratio.[13] Raman spectra of **CPQ** revealed three different bands at 2890, 2925, and 2956 cm^{-1} (Fig. S1c) for the asymmetric stretching vibration of CH_3 (methyl) groups, symmetric C-H stretching in CH_2, and asymmetric C-H stretching in CH_2 groups, respectively. The presence of many CH_2 groups in **CPQ** usually results in a stronger signal at 2925 cm^{-1} (asymmetric CH_2 stretch).[14] The PCQDs' ensuing Raman spectra widened when the **CPQ** was integrated into them. The peak intensity also decreased with a slightly lower range raman shift with the corresponding peaks of 2904, 2689, and 2561 cm^{-1}, respectively. Subtle changes in peak positions also indicate a change in the chemical environment of the C-H bonds as a result of binding or functionalization with PCQDs, while the broadening and loss of acute vibrational characteristics (Fig. S1d, e) show strong interactions between **CPQ** and the PCQDs. Additionally, it is proof that the right composite was made using a chiral agent. The Raman spectral analysis provides essential information regarding both the structural properties of pure CQDs and **CPQ**-modified CQDs.

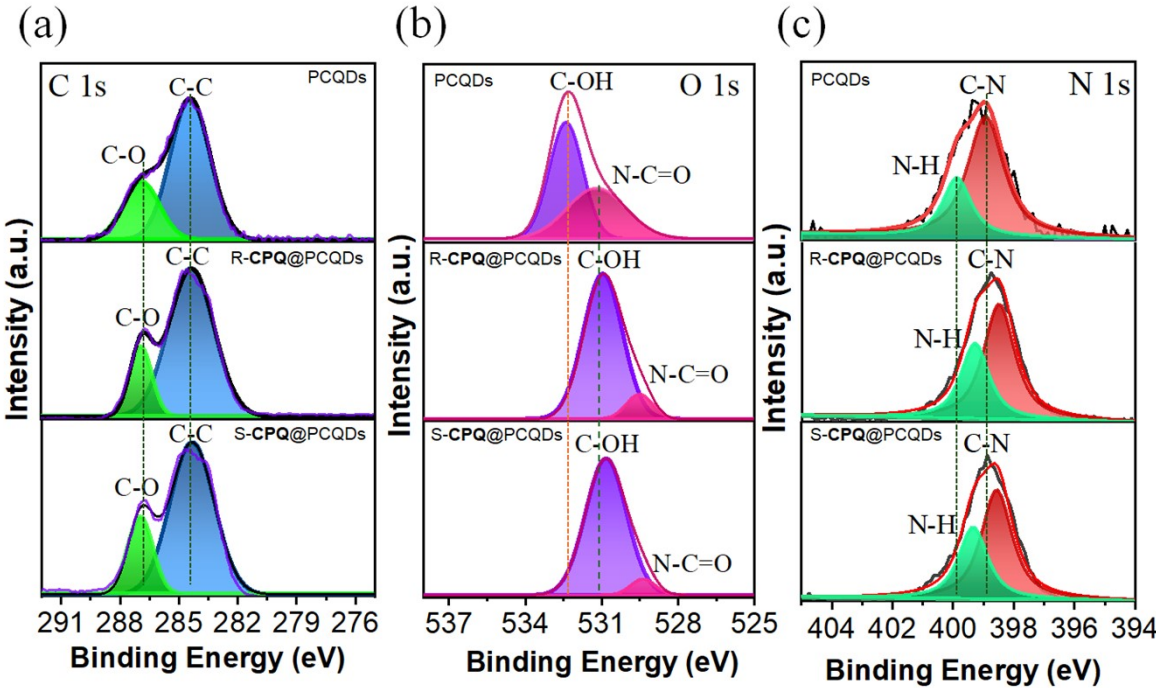

Fig. S2. (a) XPS spectra **C 1s (**PCQDs, R-**CPQ**@PCQDs, S-**CPQ**@PCQDs**),** (b) **O 1s (**PCQDs, R-**CPQ**@PCQDs, S-**CPQ**@PCQDs) and (c) **N 1s (**PCQDs, R-**CPQ**@PCQDs, S-**CPQ**@PCQDs) respectively.

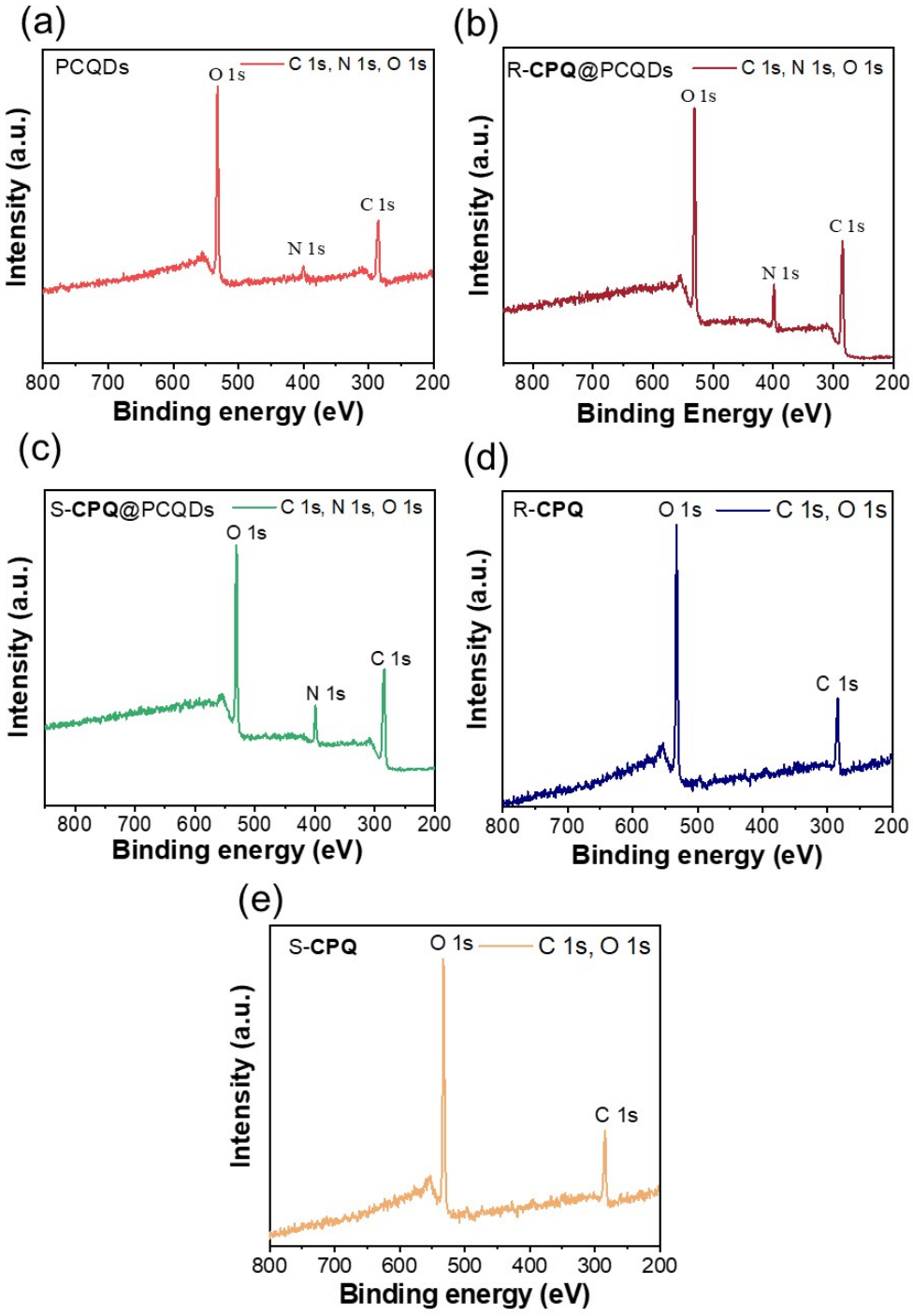

Fig. S3. Full-range XPS spectra of (a) pristine PCQDs, (b) R-**CPQ**@PCQDs, (c) S-**CPQ**@PCQDs, (d) R-**CPQ**, and (e) S-**CPQ**. Prominent peaks corresponding to C 1s, N 1s, and O 1s are observed in PCQDs and **CPQ**-functionalized PCQDs, indicating successful surface modification. The absence of N 1s peaks in R/S-**CPQ** confirms that nitrogen signals

originate from the PCQD matrix, while the enhanced O 1s intensity in R/S-**CPQ**@PCQDs suggests strong surface binding of **CPQ** ligands.

XPS was used to analyze the chemical composition of PCQDs and R/S-**CPQ**@PCQDs samples. The XPS spectra, shown in (Fig. S2a-c), detail the atomic percentages of carbon, oxygen, and nitrogen (Fig. S3 & Table S2). The C 1s peak was deconvoluted into two contributions: C–C/C=C at 284 eV and C–O/C–N at 286 eV. For R-**CPQ**@PCQDs and S-**CPQ**@PCQDs, the C–C/C=C peak showed higher binding energy compared to pure PCQDs, telling changes in the carbon bonding environment. This shift is due to a reduced electron density around carbon, leading to higher binding energy. The O 1s peak showed two bands at 531 eV (amide-O) and 532 eV (COOH). The N 1s peak contains two bands: the C-N bonding band at 398.9 eV and the N-H bonding band at 399.9 eV. The N 1s peak in R-**CPQ**@PCQDs appeared at 398.4 eV (C-N) and 399.2 eV (N-H), which showed modifications from R-**CPQ**. The N 1s spectrum of S-**CPQ**@PCQDs contained two peaks located at 398.5 eV for C-N bonds and 399.3 eV for N-H bonds. Both chiral composites demonstrated changes in their atomic environments between O 1s and N1s atoms because their ionization resulted in a local negative charge. This charge enrichment increases the electron cloud density around the oxygen and nitrogen atoms. So, the electrons experience a reduced electrostatic attraction to the nucleus. Hence, the binding energy of the O 1s and N 1s core electrons reduces. The experimental XPS data match FTIR evidence to show carboxyl and amino groups exist on PCQD surfaces to enable hydrogen bonding.[15]

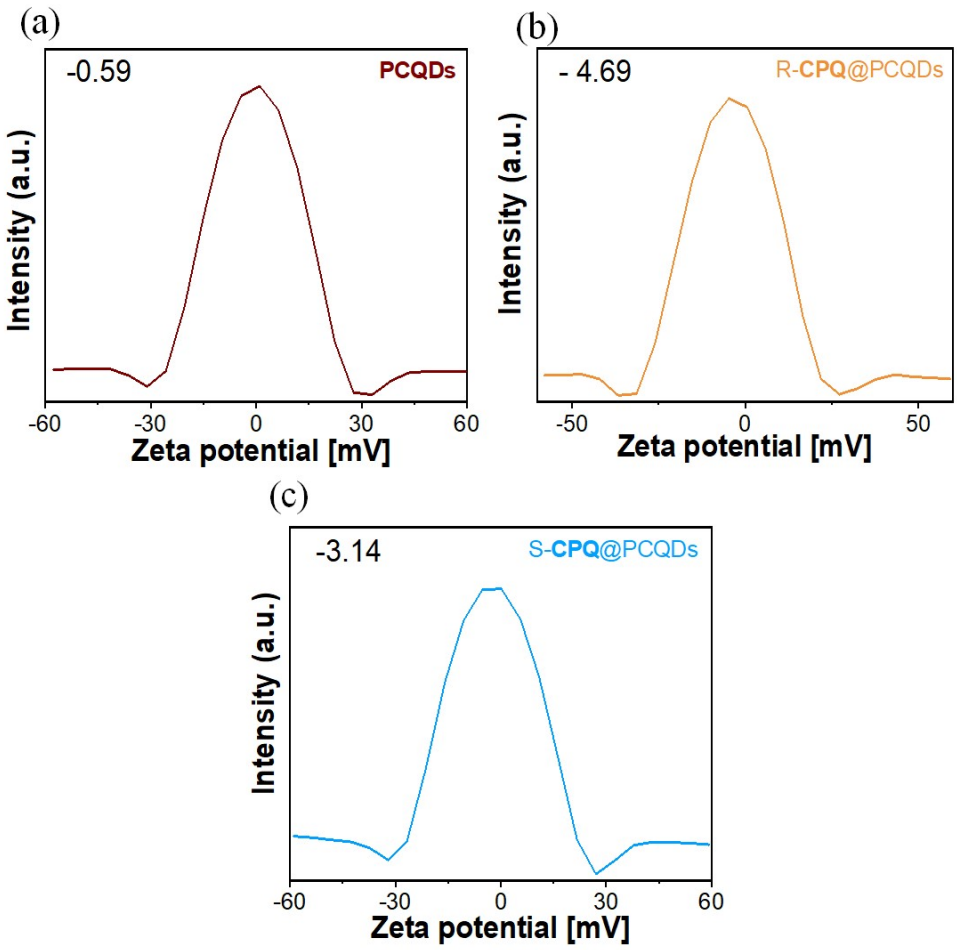

Fig. S4. Zeta potential of (a) PCQDs, (b) **R-CPQ**@PCQDs, and (c) S-**CPQ**@PCQDs.

Measuring the zeta (ζ) potential using a zetasizer provided the surface charge information related to synthesized fluorescent PCQDs. A ζ potential measurement reveals PCQD surface features together with their double layer characteristics and the hydrophilic functional groups. This measurement determines how well these produced fluorescent PCQDs can absorb ions.[16] The measured negative ζ potential emerges from PCQD particles because they possess a thick electron cloud surrounding their surface. A ζ potential value determines the long-term and short-term stability of PCQDs. The stability of CQDs depends on their ζ potential value whether it's positive or negative.[17] The ζ potential is sensitive to changes in dilution, pH, and ionic strength.[18] The ζ potential measurements yielded -0.59 mV for PCQDs and -4.69, -3.14 mV for R-**CPQ**@PCQDs and S-**CPQ**@PCQDs, respectively (Fig. S4), indicating that the lower ζ potential of the former may be due to the higher presence of electronegative atoms in its structure.[19] Hydrogen bonding and vander Waals forces exist between PCQDs and R/S-CPQ

due to the rich surface functional groups, such as -OH and -NH groups, present in their structures.[20]

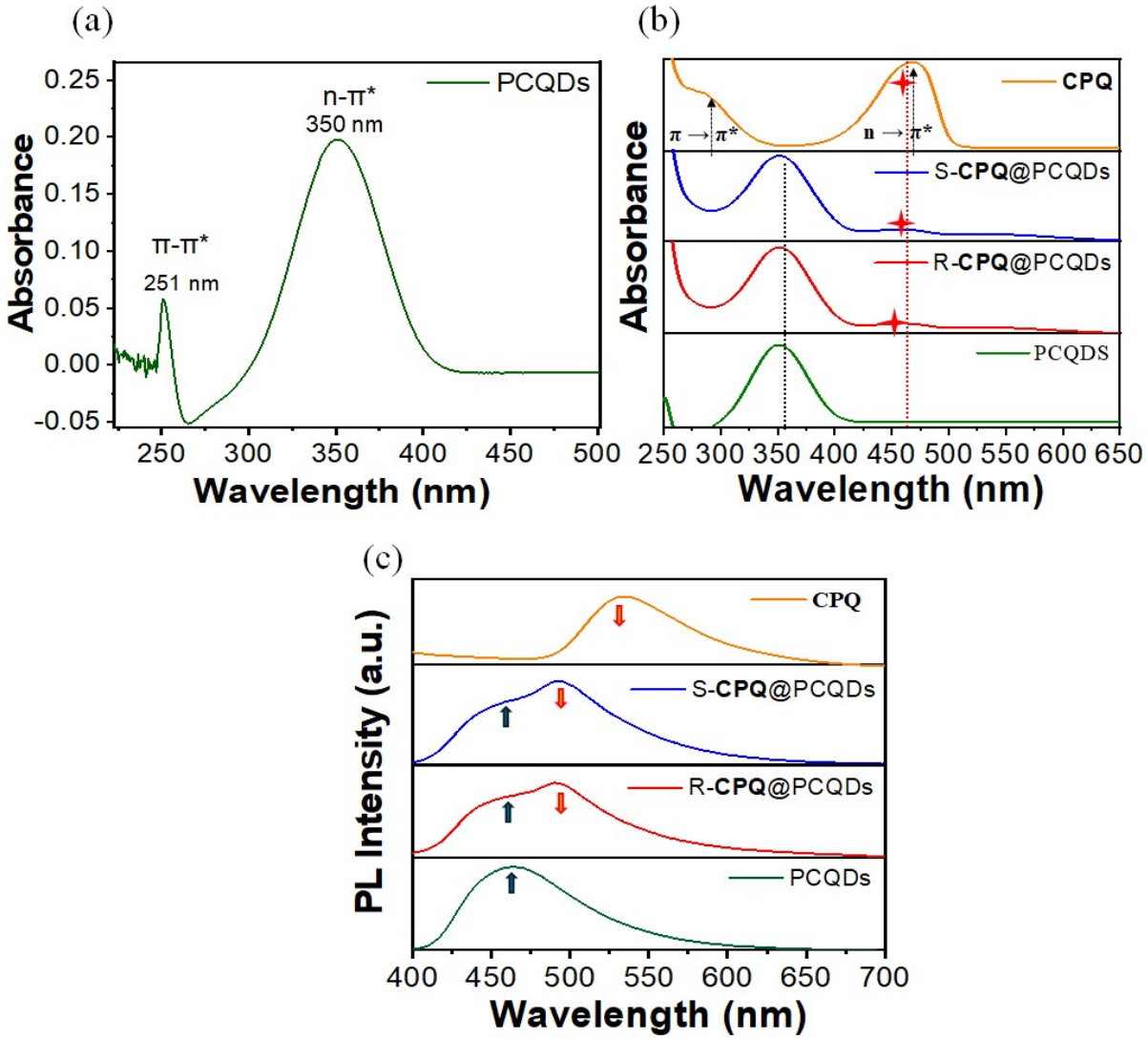

Fig. S5. (a) PCQDs show two types of electronic transitions in the absorbance spectrum, (b) Absorption spectra PCQDs, R-**CPQ**@PCQDs, S-**CPQ**@PCQDs, **CPQ** , (c) PL spectra for PCQDs, R-**CPQ**@PCQDs, S-**CPQ**@PCQDs, CPQ; λ_{ex} = 350 nm.

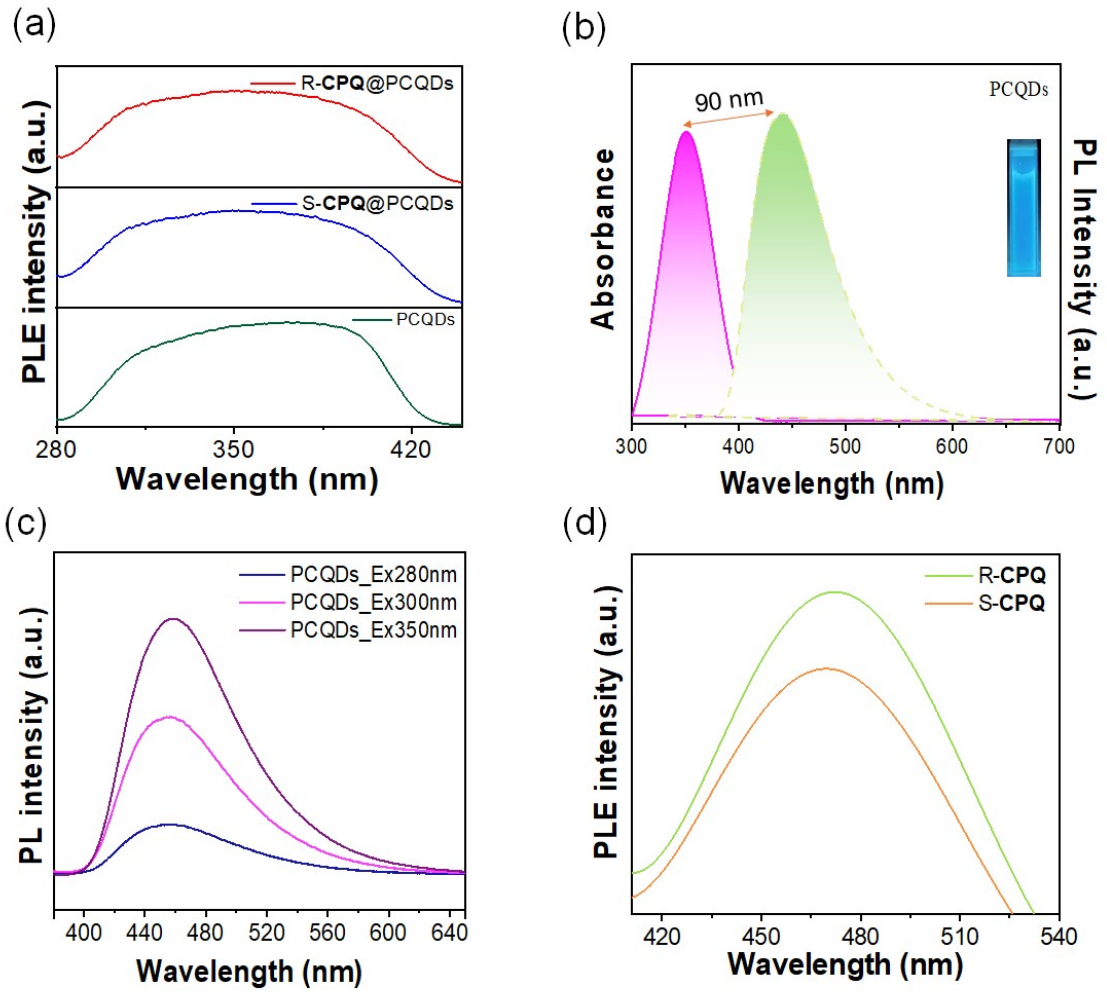

Fig. S6. (a) PLE of PCQDs, R-**CPQ**@PCQDs, and S-**CPQ**@PCQDs, (b) Stokes shift of pure carbon dots, (c) Excitation-dependent PL of PCQDs, (d) PLE spectra of R/S-**CPQ**

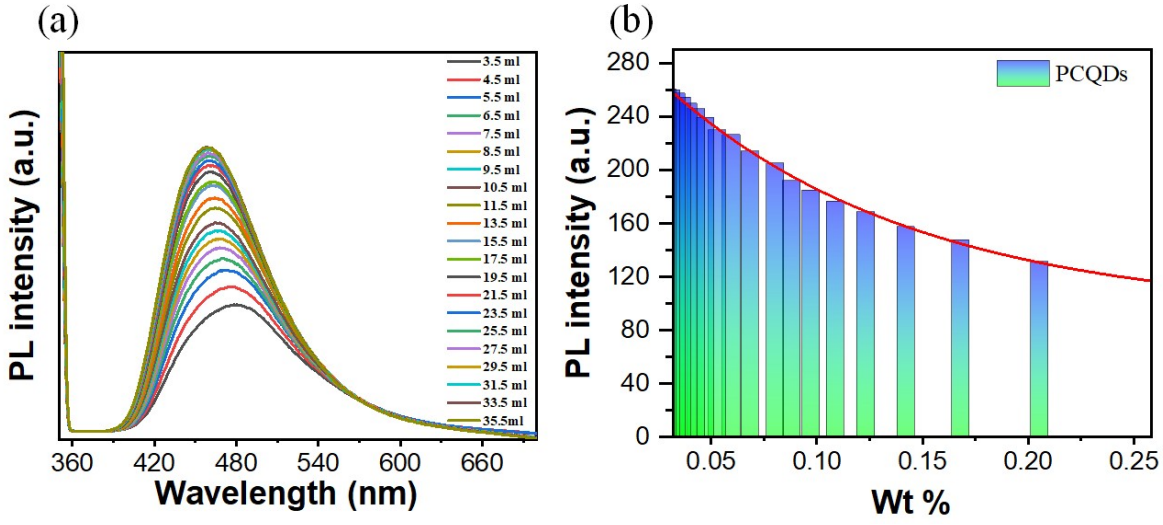

Fig. S7. (a) Photoluminescence (PL) spectra of PCQDs recorded at an excitation wavelength of 350 nm as a function of concentration, (b) Bar chart illustrating the variation in PL intensity of PCQDs with respect to different weight percentages (wt%).

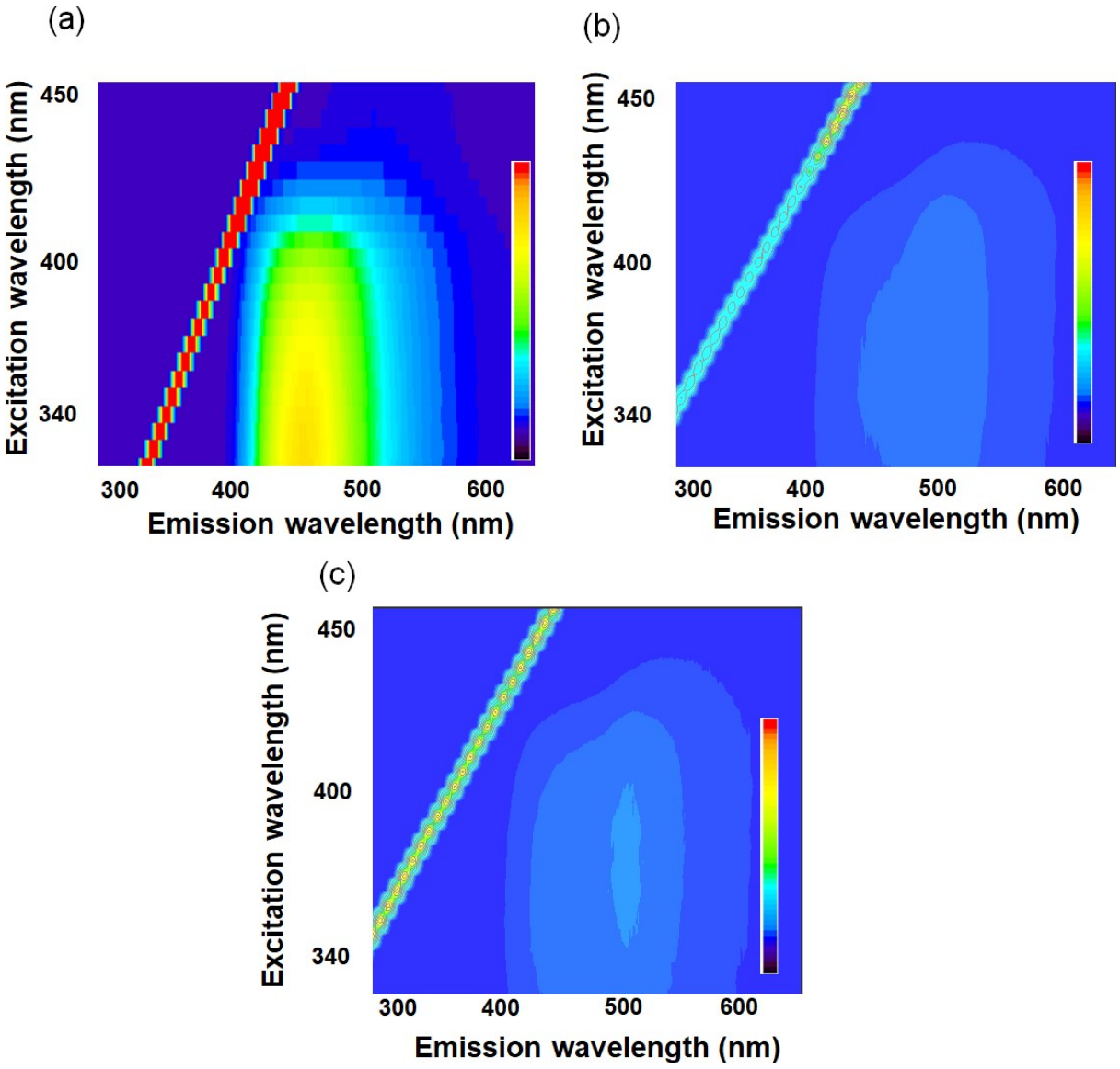

Fig. S8. 3D PL-mapping for (a) pure PCQDs, (b) R-**CPQ**@PCQDs**,** and (c) S-**CPQ**@PCQDs at different excitation and emission.

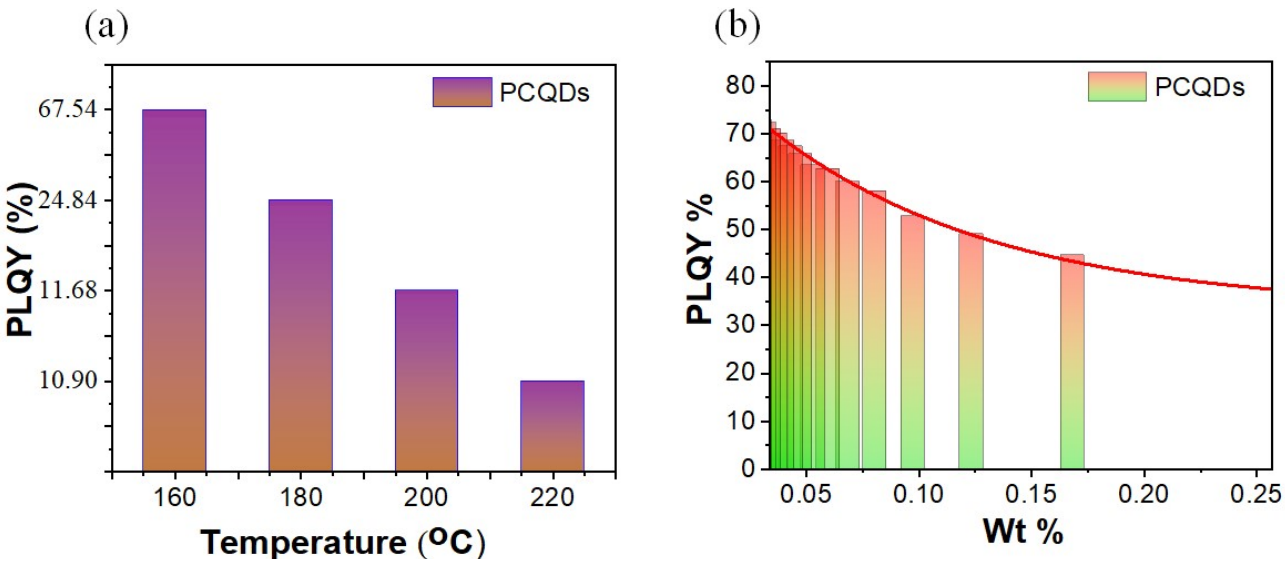

Fig. S9. (a) PL QY of PCQDs at different synthesizing temperatures, explaining thermal effects on emission efficiency, (b) Bar plot of PL QY as a function of PCQD weight percentage (wt%), showing the impact of concentration on PL QY.

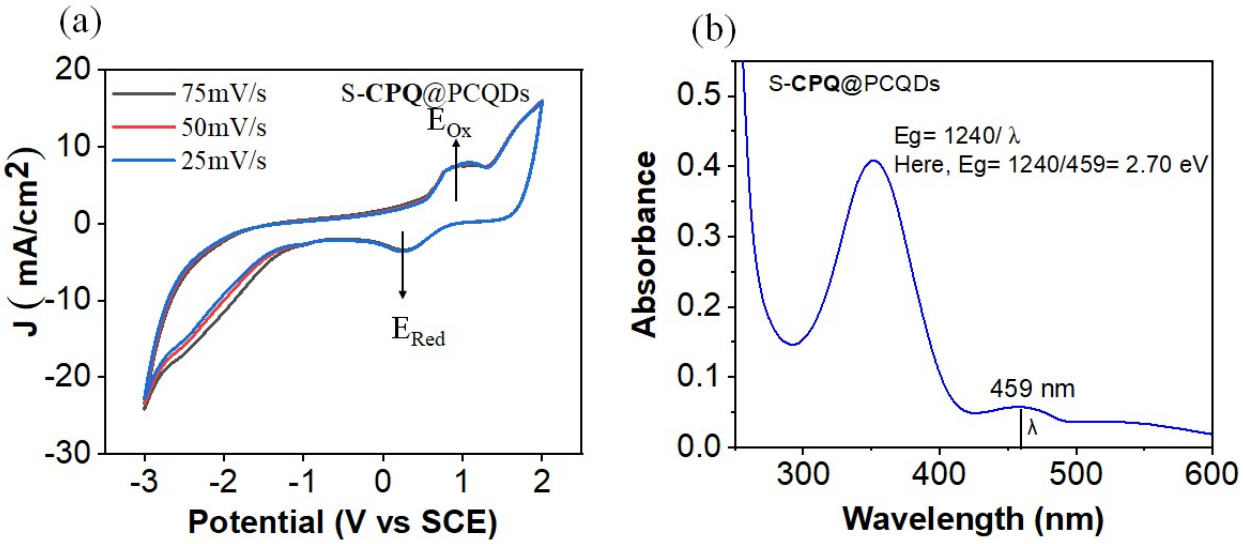

Fig. S10. (a) Cyclic voltammetry curves of S-**CPQ**@PCQDs recorded at scan rates of 25, 50, and 75 mV/s reveal distinct redox features. The onset oxidation and reduction potentials were used to estimate the electrochemical HOMO-LUMO gap, (b) The optical bandgap (E_g) was determined from the absorption spectrum, providing complementary insight into the electronic structure of S-**CPQ**@PCQDs.

Cathodic reduction (E_c) = 0.28V

Oxidation Anode (E_a) = 0.95V

$$E_{1/2red} = \frac{(E_a + E_c)}{2} = \frac{0.95 + 0.28}{2} = 0.615 \text{ V}$$

$$E_{HOMO} = -e[E_{1/2red} + 4.4\,V] \text{ (ferrocene value of -4.4 eV)}$$

$$= -5.01_V$$

$$E_{LUMO} = E_{HOMO} + E_g(optical)$$

$$E_g = \frac{1240}{\lambda} = 2.7\ eV\ (calculated\ from\ Fig.\ S12b)$$

$$E_{LUMO} = -5.01eV + 2.70\ ev = -2.31\ eV$$

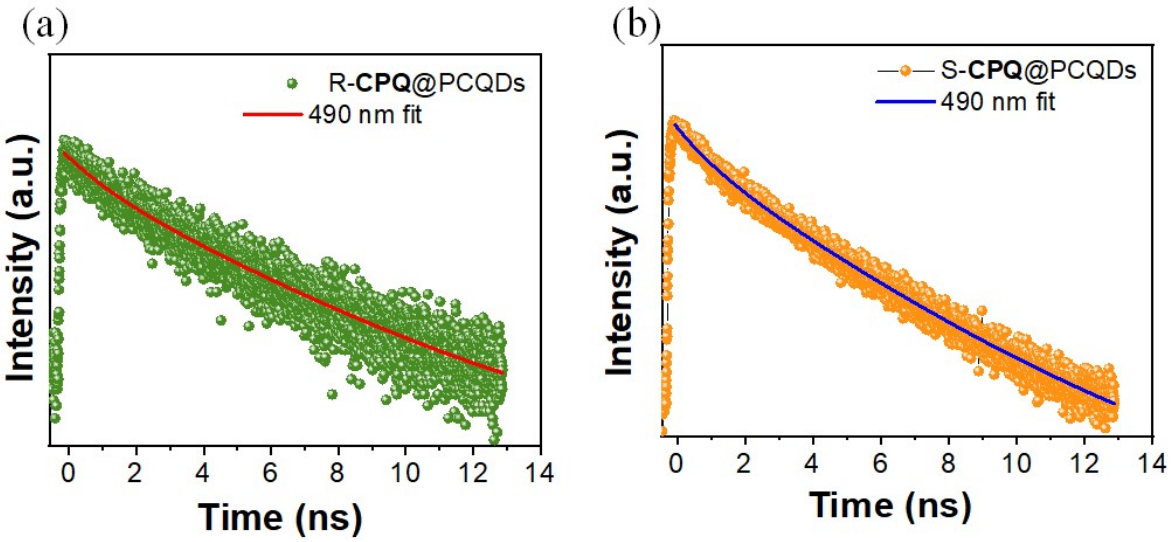

Fig. S11. (a) TRPL spectra of R-**CPQ**@PCQDs, (b) TRPL spectra of S-**CPQ**@PCQDs recorded at 490 nm emission wavelength, fitted with biexponential decay models (solid lines). Both samples show nanosecond-scale emission lifetimes, with discernible differences in decay kinetics indicative of chiral-dependent carrier dynamics or surface passivation efficiency.

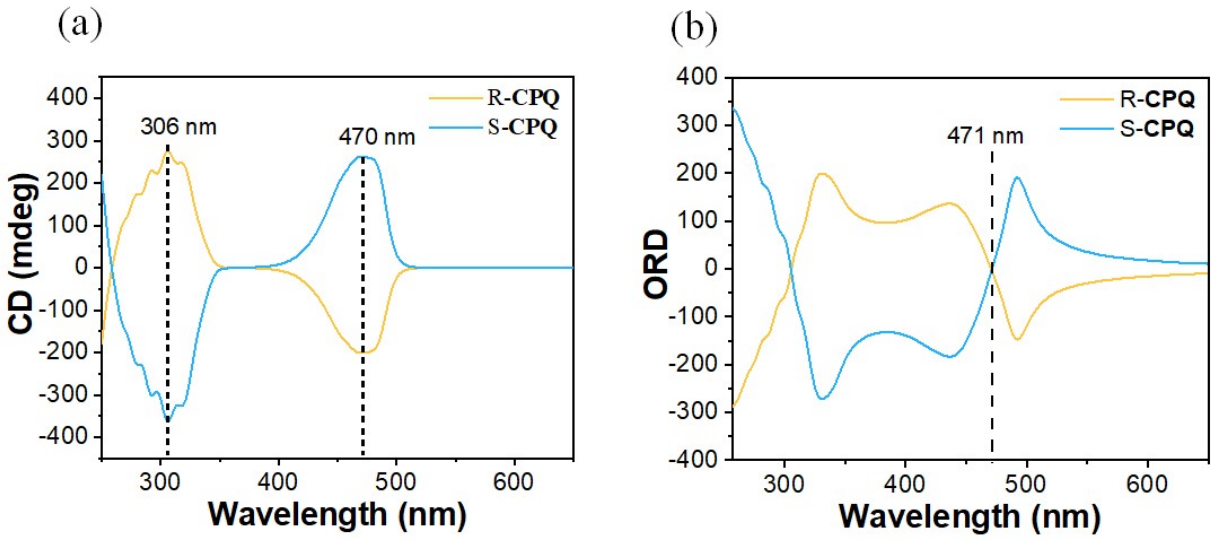

Fig. S12. (a) CD spectra of R-**CPQ** and S-**CPQ**, (b) ORD spectra of R-**CPQ** and S-**CPQ**. The specific features of the CD spectrum of R/S-**CPQ** are a result of the complex 3D arrangement of its atoms, which leads to different electronic transitions for LCP and RCP light. These transitions are associated with the energy differences between electronic states in the molecule. The exact positions and intensities of the peaks depend on the precise arrangement of the atoms and the electronic structure of the molecule.

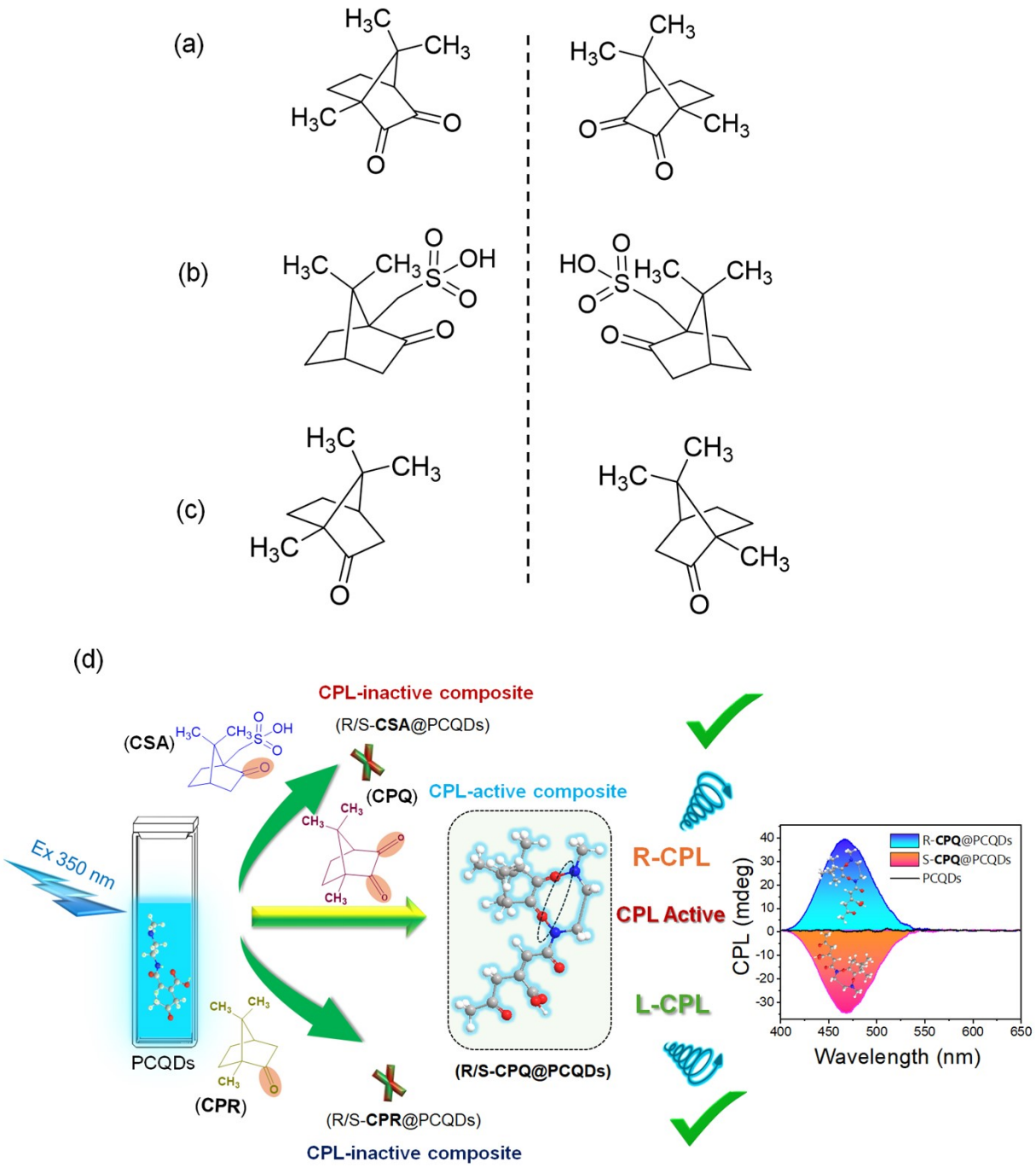

Fig. S13. Stereoisomeric structure of (a) R/S-**CPQ,** (b) R/S-**CSA**, (c) R/S-**CPR**, (d) Supramolecular chirality induction in PCQDs and their CPL activity. Schematic illustration showing the interactions between PCQDs and different camphor derivatives (**CPQ**, **CSA**, and **CPR**). When excited at 350 nm, PCQDs complexed with R/S-**CPQ** demonstrate distinct CPL activity through supramolecular hydrogen bonding (center), whereas PCQDs modified with (R/S-**CSA**@PCQDs) or (R/S-**CPR**@PCQDs) show no CPL signal. The molecular structure in the center depicts the hydrogen bonding network between PCQDs and **CPQ** that enables

chirality transfer. The graph on the right shows the mirror-image CPL signals of R-**CPQ**@PCQDs and S-**CPQ**@PCQDs, confirming successful chirality induction.

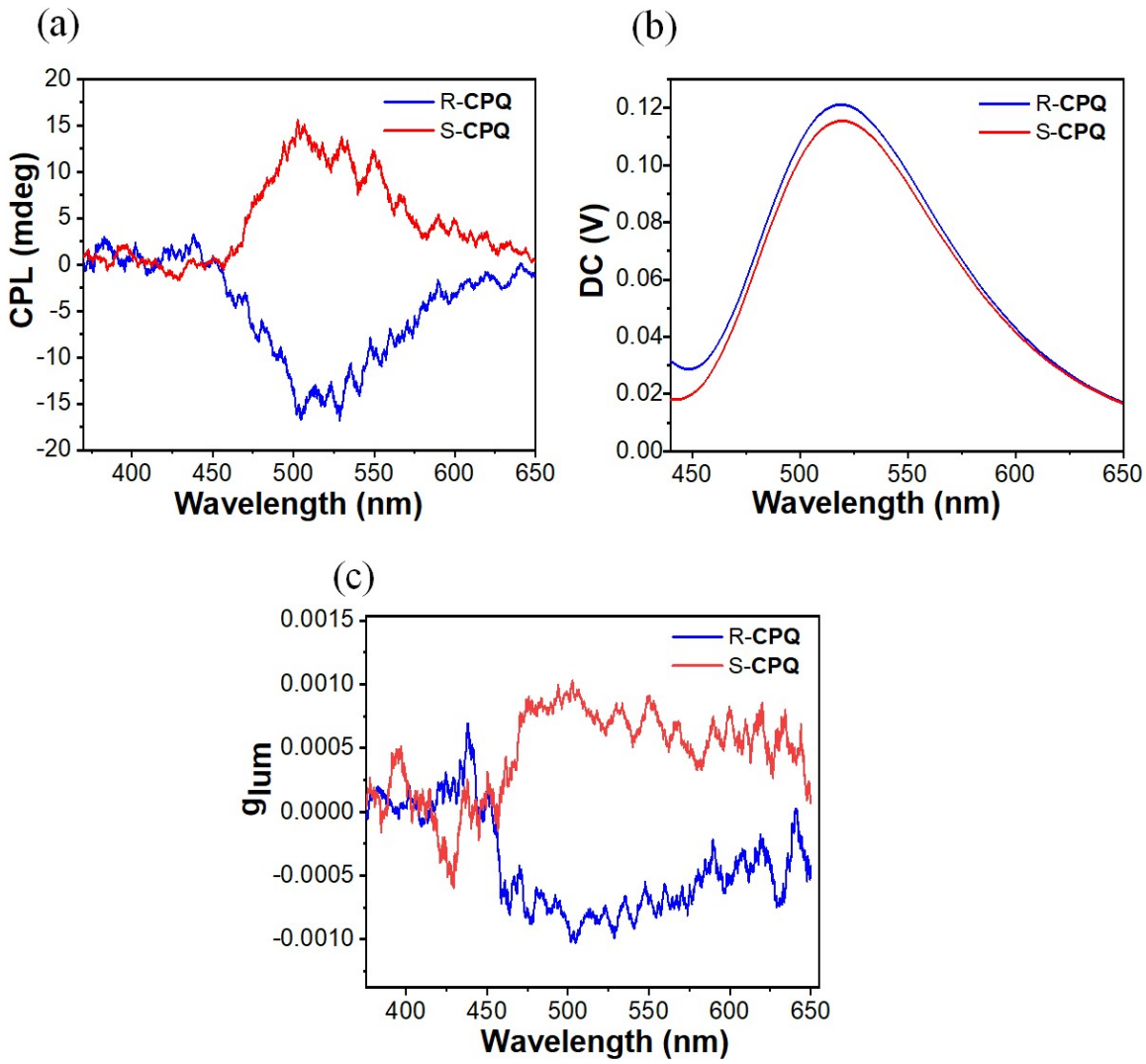

Fig. S14. (a) CPL spectra for R-**CPQ** and S-**CPQ**, (b) Direct current **(**DC) of R-**CPQ** and S-**CPQ**, (c) Luminescence dissymmetry factor (g_{lum}) of R-**CPQ** and S-**CPQ** in ethanol.

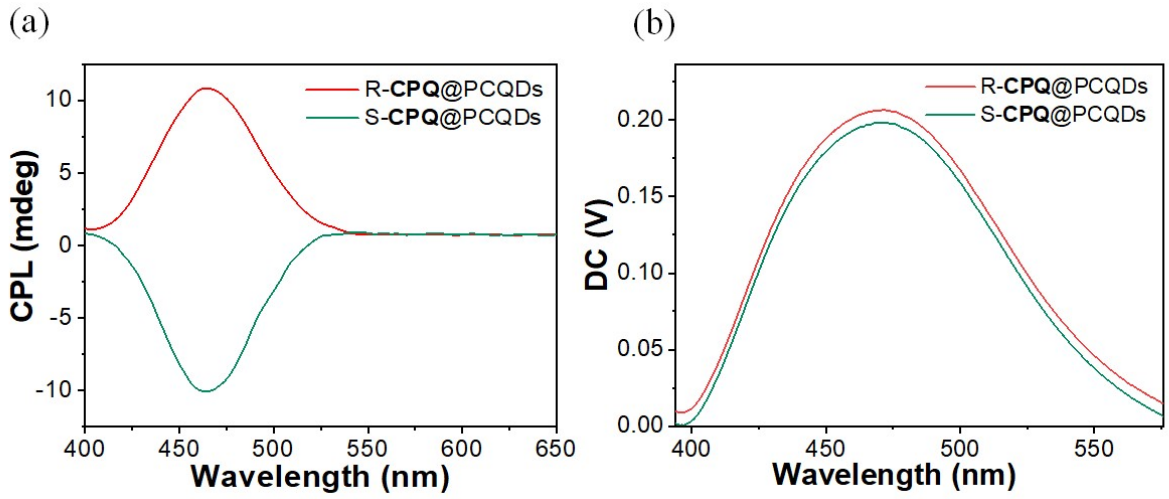

Fig. S15. (a) CPL spectra of R/S-**CPQ**@PCQDs, (b) Direct current (DC) R/S-**CPQ**@PCQDs was recorded for saturated solution at λ_{ex} = 350 nm.

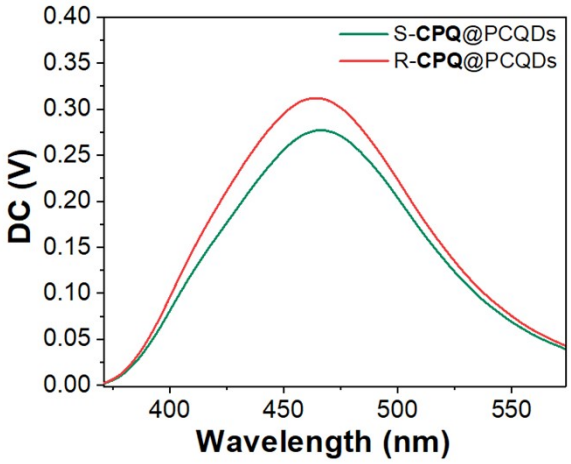

Fig. S16. Direct current (DC) response (corresponding to Fig. 4c) as a function of wavelength for R/S-**CPQ**@PCQDs. Both enantiomer-functionalized PCQD systems reveal a peak response near 463 nm. The spectral behavior suggests chiroptical modulation of the local electric field, potentially arising from asymmetric charge distribution induced by chiral surface interactions

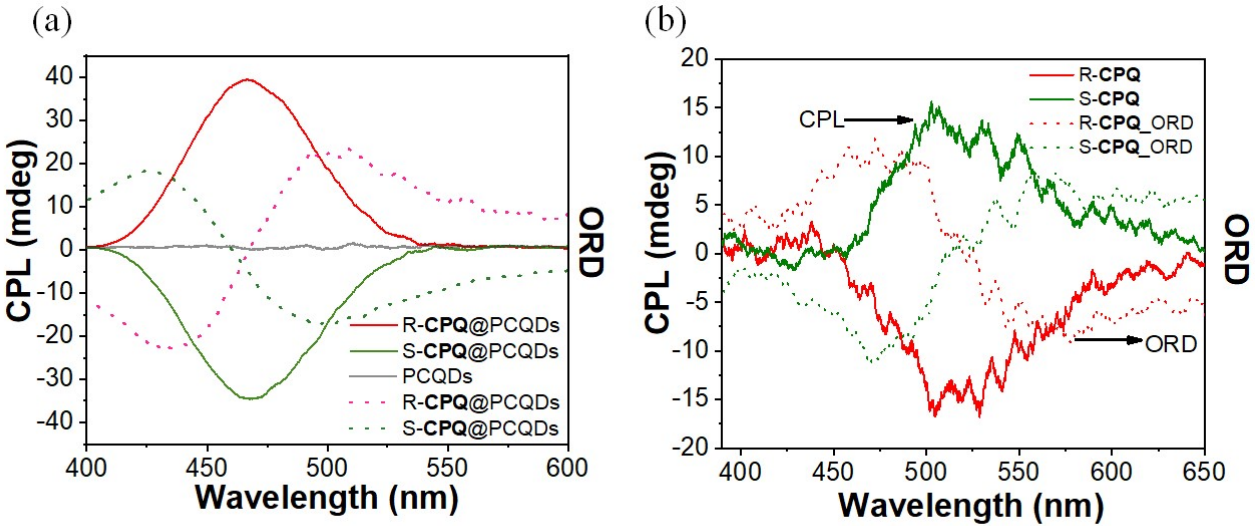

Fig. S17. (a) CPL and ORD spectra of R-**CPQ**@PCQDs and S-**CPQ**@PCQDs showing complementary chiroptical responses, (b) Comparative overlay of CPL and ORD spectra for pure R-**CPQ** and S-**CPQ**, illustrating how supramolecular assembly with PCQDs modifies the chiroptical properties. The direct relationship between CPL emission and ORD behavior confirms the fundamental connection between light emission and rotation phenomena in these chiral systems.

The connection between CD and ORD can be understood through the Kramers-Kronig relations, which mathematically connect the real (n) and imaginary (k) parts of a material's refractive index (see Equation S5). The CPL signals of the COBCs show zero-crossings that align with inflection points in their corresponding ORD spectra, revealing a clear manifestation of the Kramers-Kronig relation between emission and dispersion in chiral systems. The derivative-like ORD profiles mirror CPL features, indicating a coherent interplay between circularly polarized absorption and emission. This correlation affirms that the observed chirality arises from intrinsic modifications in the electronic structure, rather than surface-limited effects.

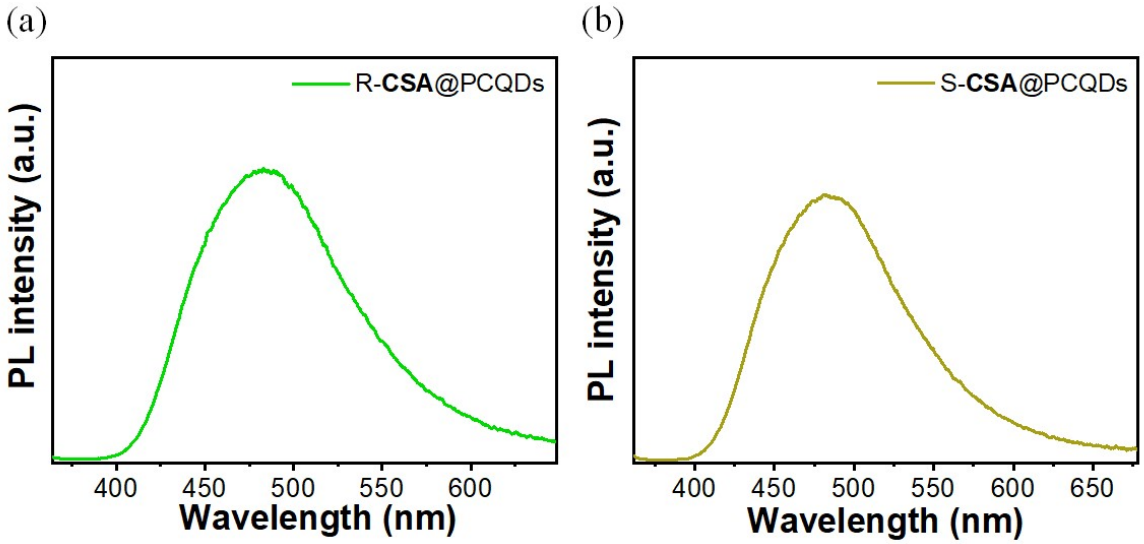

Fig. S18. Photoluminescence (PL) intensity of R-**CSA**@PCQDs (a), S-**CSA**@PCQDs (b) under λ_{ex} = 350 nm.

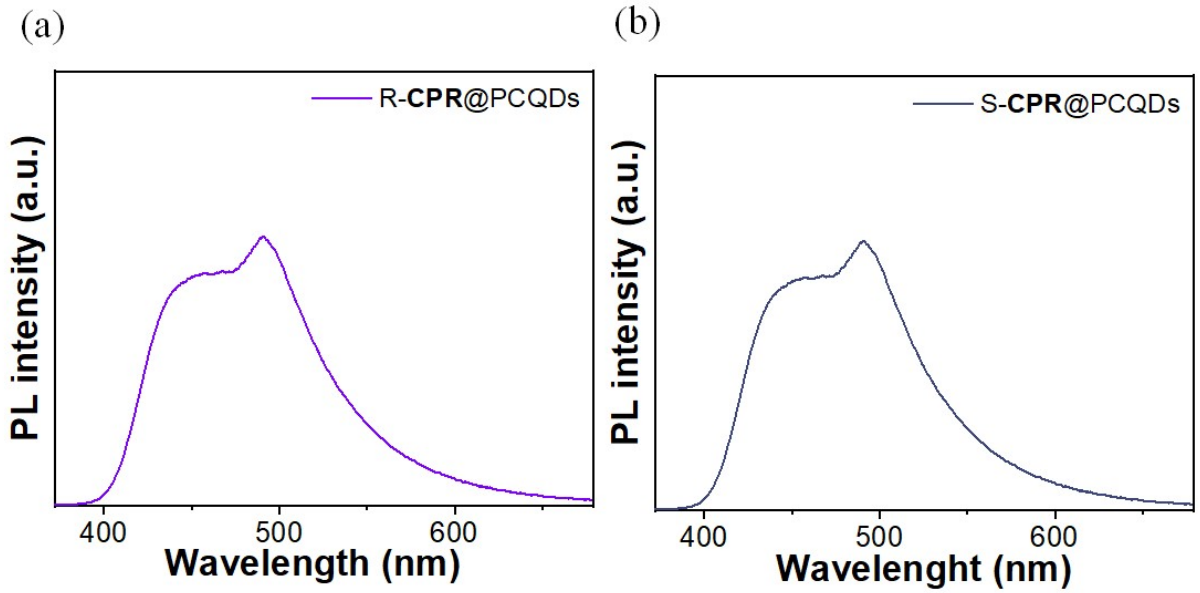

Fig. S19. PL intensity of (a) R-**CPR**@PCQDs, and (b) S-**CPR**@PCQDs at λ_{ex} = 350 nm.

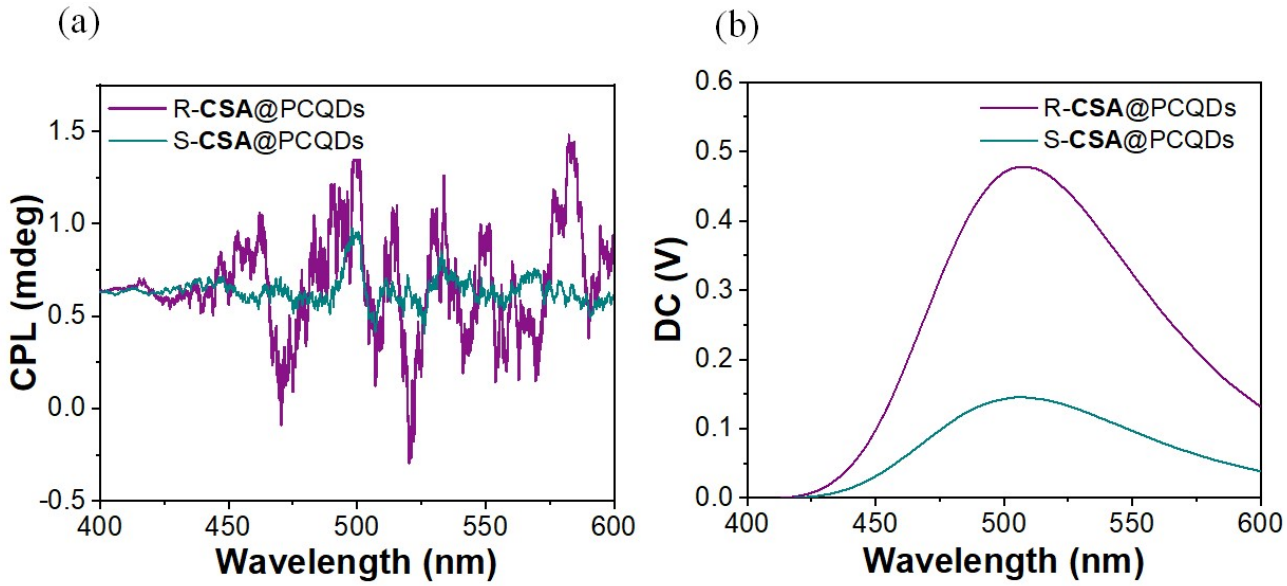

Fig. S20. (a) CPL spectra of R-**CSA**@PCQDs and S-**CSA**@PCQDs, (b) Direct current (DC) of R/S-**CSA**@PCQDs at λ_{ex} = 350 nm.

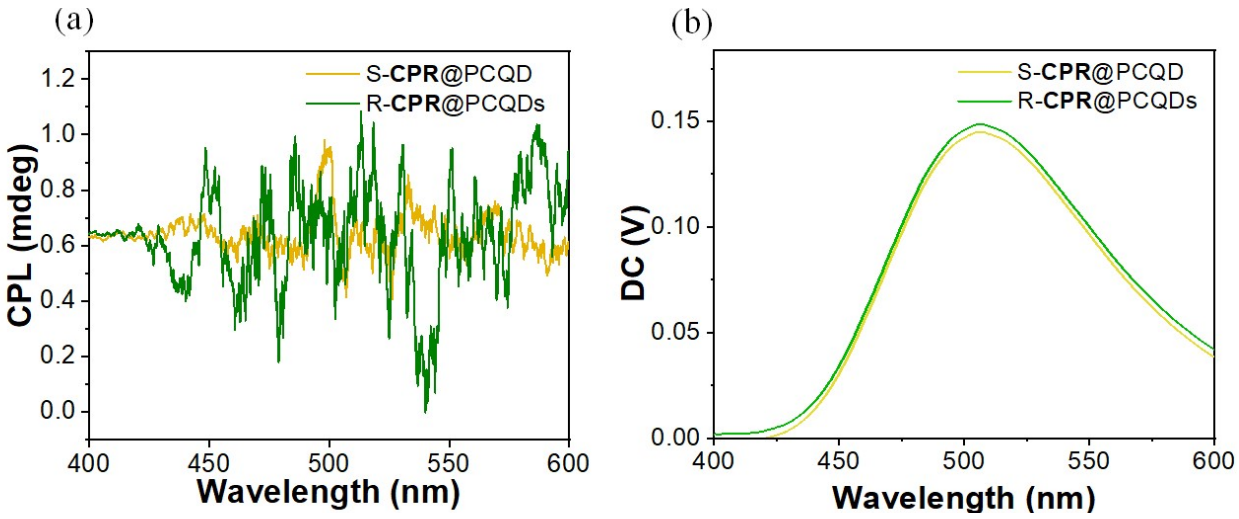

Fig. S21. (a) CPL spectra of R/S-**CPR**@PCQDs, (b) Direct current (DC) of R/S-**CPR**@PCQDs at λ_{ex} = 350 nm.

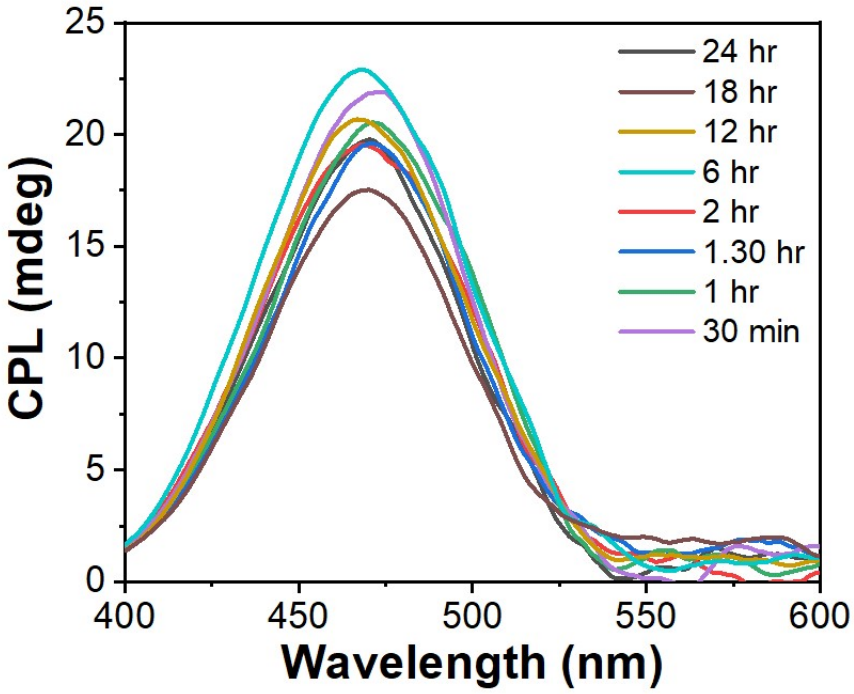

Fig. S22. Photostability of R-CPQ@PCQDs under continuous UV irradiation (365 nm). CPL spectra recorded at different exposure times show negligible change in spectral shape and peak position, with only a slight decrease in intensity, confirming good resistance to photobleaching.

Fig. S23. Photograph of R-CPQ@PCQDs dispersed in an H_2O/EtOH mixture under ambient light (left) and UV illumination (365 nm), showing bright and spatially uniform blue emission, confirming good colloidal stability under CPL measurement conditions.

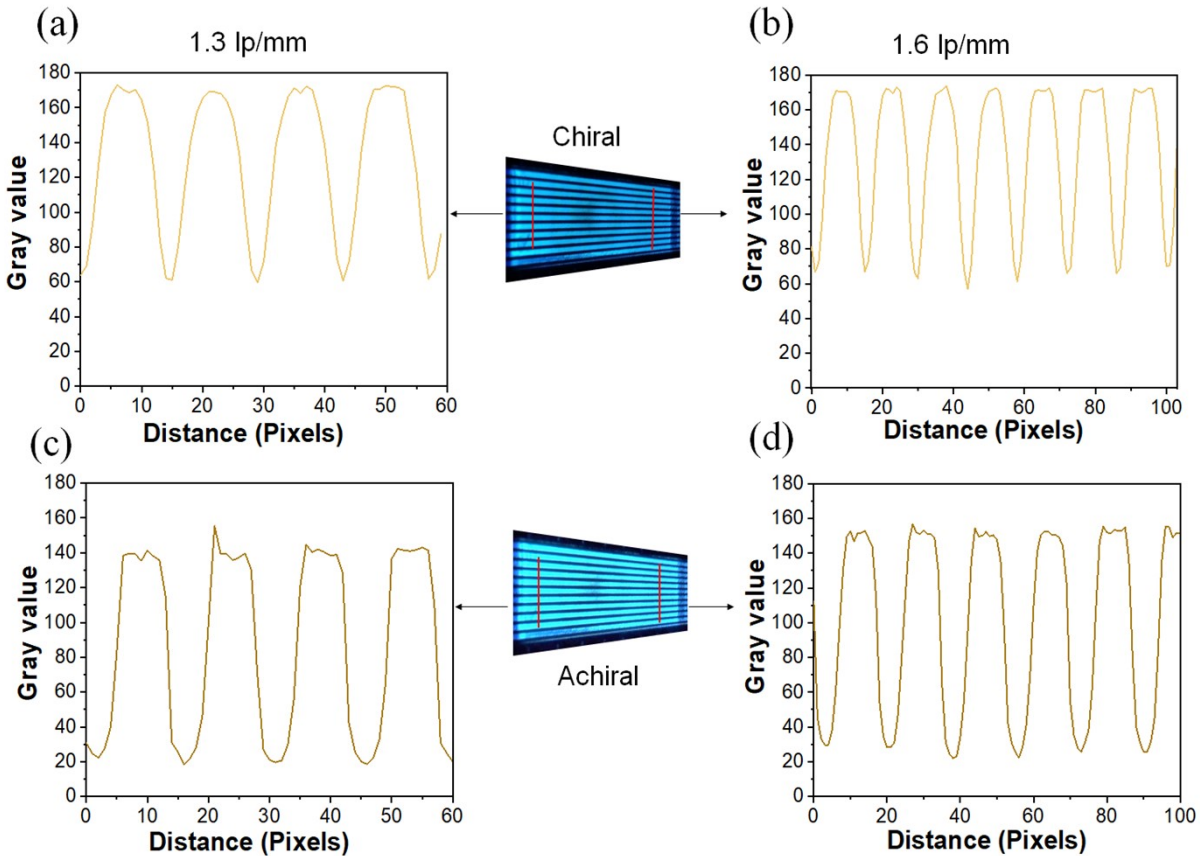

Fig. S24. Spatial resolution assessment of chiral R/S-CPQ@PCQDs (a,b), and achiral PCQDs (c,d)**.** Line pair patterns at spatial frequencies of 1.3 and 1.6 lp/mm were used to evaluate the imaging performance of the chiral R/S-**CPQ**@PCQDs compared to achiral PCQDs.

Supplementary Tables

Table S1. The summary of reported chiral carbon dots and their corresponding g_{lum} values.

Study	Chiral source	λ_{ex} , λ_{em}	g_{lum}	Year
Chiral carbon dots	L-/D-Tartaric Acid	-	-	2016[21]
Chiral N-S-doped Carbon	L-/D-Cysteine	300 nm, 510 nm	-	2018[22]
Chiral Fluorescent Carbon Nanodots	L-/D-Tryptophan	363 nm, 476 nm	-	2019[23]
Chiral-CQDs from cellulose NCs	Cellulose	380 nm, 461 nm	-2×10^{-1}	2020[24]
Chirality Transfer in Carbon Dot-Composited Sol−Gel	L/ DGAm	365 nm, 445 nm	10^{-4}	2020[25]
CPL of $CsPbX_3$ Nanocrystals Triggered by Chiral CDs	L/D-Serine	338 nm, 445 nm	-3.1×10^{-3}	2022[26]
Chiral Carbon dots in Bi-Solvent	Thioflavin T (ThT)	385 nm, 424 nm	10^{-3}	2022[15]
Self-Assembly of Cholesteryl Carbon Dots	cholesteryl periphery	324 nm, 450 nm	10^{-3}	2023[27]
Transmitting biomolecular chirality into carbon nanodots	L- or D-cysteine	350 nm, 450 nm	7×10^{-4}	2023[28]
Amplification of Intrinsic Circularly Polarized Room Temperature Phosphorescence in	(R/S)-1,1′-binaphthyl-2,2′-diamine	400 nm, 460 nm	10^{-3}	2024[29]

Chiral Carbon Dots				
Construction of Carbon Dot-Based Color-Tunable Circularly Polarized	l/d-arginine	458, 510, 547 nm, 494-642 nm	10^{-4}	2025[30]
All-organic chiral liquid polarizer of the polymeric carbon dot for minimizing optical crosstalk	**R/S-CPQ@PCQDs**	**350 nm ,463 nm**	**$\pm 1.42 \times 10^{-2}$**	**2025 (our work)**

Table S2. Chemical composition of three PCQDs (achiral and COBCs) and R/S-CPQ samples determined from XPS data.

Sample	C, %	O, %	N, %
PCQDs	45.5	48.3	6.2
R-**CPQ**@PCQDs	58.2	31.5	10.3
S-**CPQ**@PCQDs	57.3	32.4	10.3
R-**CPQ**	48.3	51.7	
S-**CPQ**	45	55.0	

Table S3. Average photoluminescence lifetimes derived from TRPL analysis of PCQDs and chiral-functionalized derivatives. which provide essential insights into the photophysical properties of these materials.

Sample	B_1	B_2	τ_1	τ_2	$\tau_{avg}=\Sigma\alpha_i\tau_i^2/\Sigma\alpha_i\tau_i$
PCQDs	0.395	0.045	0.45	7.25	4.85
R-**CPQ**@PCQDs	0.187	0.0373	0.93	5.59	3.46
S-**CPQ**@PCQDs	1.155	0.255	0.98	5.99	3.85

References

1 H. Chakraborty and B. R. Lentz, *Biochemistry.*, 2012, **51**, 1005–1008.

2 A. Döring, E. Ushakova and A. L. Rogach, *Light Sci Appl.*, 2022, **11**, 1–23.

3 L. Wan, R. Zhang, E. Cho, H. Li, V. Coropceanu, J. L. Brédas and F. Gao, *Nat Photonics.*, 2023, **17**, 649–655.

4 K. F. Lee, K. M. Luk and H. W. Lai, *Microstrip Patch Antennas.*, 2nd edn, 2017, **459–525**.

5 C. Jiang, C. Jin, Y. Lv, X. Han, Z. Li, Z. Liu, Q. Yan, Y. Liu, S. Dai, D. Li and Y. Cui, *J. Am. Chem. Soc.*, 2026, **148**, 2551–2562

6 M. Bass (ed.), Handbook of Optics, Vol. I, 2nd edn, *McGraw-Hill, New York, NY*, 1995, p. **247-277**.

7 J. P. Riehl and F. S. Richardson, *Chem Rev.*, 1986, **86**, 1–16.

8 A. Sillen and Y. Engelborghs, *Photochem. Photobiol.*, 1998, **67**, 475–486.

9 M. K. Barman, B. Jana, S. Bhattacharyya and A. Patra, *J Phys Chem C.*, 2014, **118**, 20034–20041.

10 L. Fu, Y. Yin, G. Cao, P. Wu, J. Wang, L. Yan, B. Zhang and M. Li, *Chinese Phys B*, 2019 *Chinese Phys. B.*, **28**, 128102.

11 K. M. Omer, D. I. Tofiq and A. Q. Hassan, *Microchim Acta.*, 2018, **185**, 4–11.

12 A. Kelarakis, *MRS Energy Sustain.*, 2014, **1**, 1–15.

13 X. Wang, P. Yang, Q. Feng, T. Meng, J. Wei, C. Xu and J. Han, *Polymers (Basel).*, 2019, **11**, 616.

14 R. Lu, W. Gan, B. H. Wu, Z. Zhang, Y. Guo and H. F. Wang, *J Phys Chem B.*, 2005, **109**, 14118–14129.

15 Z. Zhang, C. Yang, Y. Dai, X. Zhang, J. Chen and L. Feng, *A Eur J.*, 2022, **28**, e202202589.

16 M. Y. Pudza, Z. Z. Abidin, S. A. Rashid, F. M. Yasin, A. S. M. Noor and M. A. Issa, *Nanomaterials.*, 2020, **10**, 315.

17 W. Li, S. Wang, Y. Li, C. Ma, Z. Huang, C. Wang, J. Li, Z. Chen and S. Liu, *Carbohydr Polym.*, 2017, **175**, 7–17.

18 J. D. Clogston and A. K. Patri, *Methods Mol Biol.*, 2011, **697**, 63–70.

19 Y. Takayama, H. Negishi, S. Nakamura, N. Koura, Y. Idemoto and F. Yamaguchi, *J Ceram Soc Japan.*, 1999, **107**, 119–122.

20 H. Zheng, B. Ju, X. Wang, W. Wang, M. Li, Z. Tang, S. X. A. Zhang and Y. Xu, *Adv Opt Mater.*, 2018, **6**, 1–7.

21 Y. Yu, W. Liu, J. Ma, Y. Tao, Y. Qin and Y. Kong, *RSC Adv.*., 2016, **6**, 84127–84132.

22 F. Li, Y. Li, X. Yang, X. Han, Y. Jiao, T. Wei, D. Yang, H. Xu and G. Nie, *Angew Chemie - Int Ed*, 2018, **57**, 2377–2382.

23 Y. Wei, L. Chen, J. Wang, X. Liu, Y. Yang and S. Yu, *RSC Adv.*, 2019, **9**, 3208–3214.

24 M. Chekini, E. Prince, L. Zhao, H. Mundoor, I. I. Smalyukh and E. Kumacheva, *Adv Opt Mater.*, 2020, **8**, 1–9.

25 A. Li, D. Zheng, M. Zhang, B. Wu and L. Zhu, *Langmuir.*, 2020, **36**, 8965–8970.

26 Y. Ru, B. Zhang, X. Yong, L. Sui, J. Yu, H. Song and S. Lu, *Adv Mater.*, 2023, **35**, 1–9.

27 K. Yin, N. Feng, N. Godbert, P. Xing and H. Li, *J Phys Chem Lett.*, 2023, **14**, 1088–1095.

28 S. Maniappan, K. L. Reddy and J. Kumar, *Chem Sci.*, 2022, **14**, 491–498.

29 X. Gao, K. Pan, B. Zhao and J. Deng, *Adv Funct Mater.*, 2024, **2413569**, 1–13.

30 Y. Wang, S. Zhou, Y. Zhao, H. Xiao, L. B. Xing, X. Sun, J. Zhou and S. Lu, *Nano Lett.*, 2025, **25**, 4060–4067.